Proceedings of the
ASIAN RESEARCH ASSOCIATION

Electrochemical Properties of Ferrous Nickel Pyrophosphate Thin Film Electrodes for Energy Storage Applications

S. Nivetha [a, *], S. Prabahar [a], R.T. Karunakaran [a], M. Narendhera Ganth [a], T. Boobalan [b], S. Dhinesh [c]

[a] Department of Physics, Government Arts College, Udumalpet-642126, Tamil Nadu, India
[b] Westechpower Management Pvt Ltd, Pune- 411062, Maharastra, India
[c] Department of Physics, M. Kumarasamy College of Engineering (Autonomous), Karur-639113, Tamil Nadu, India
* Corresponding author Email: nivethasr267@gmail.com
DOI: https://doi.org/10.54392/ara2417
Received: 11-05-2024; Revised: 09-07-2024; Accepted: 16-07-2024; Published: 30-07-2024

Abstract: The present work deals with the preparation of ferrous nickel pyrophosphate ($Fe_2Ni_2P_2O_7$) thin films via a facile approach namely chemical bath deposition. X-ray diffraction analysis evinces that the prepared $Fe_2Ni_2P_2O_7$ thin films are of monoclinic structure and crystallinity is improved by increase in Fe concentration with a preferential orientation along the (111) direction. Scanning electron microscopy and high-resolution scanning electron microscopy analysis reveal the microsphere like morphology and uniform anchoring of Fe_2 on $Ni_2P_2O_7$ thin film surface, which is favorable for good charge transfer between the electrode and electrolyte interface. The UV-Visible spectroscopy analysis reveals that direct optical band gap of $Fe_2Ni_2P_2O_7$ thin films holds decreasing trend from 3.80 eV to 3.17 eV with increasing amount of Fe from 1M to 3M. Photoluminescence spectroscopy has been employed to study the luminescence properties, with respect to the Fe concentration. The different phonon modes and magnon modes of vibration present in the $Fe_2Ni_2P_2O_7$ film have been studied by Raman spectroscopy. Electrochemical analysis shows that, the $Fe_2Ni_2P_2O_7$ film electrode offers a specific capacitance of 441 F/g with excellent electrochemical and cyclic stability. The studies on $Fe_2Ni_2P_2O_7$ films have yielded promising results enrich express the potentiality for better utilization in energy storage devices.

Keywords: Optical properties, Luminescence, CBD, Energy storage

1. Introduction

In recent years, the world concern about the efficient energy storage systems in order to meet out their requirements from high power electric vehicles to commercial electronics devices. In this aspect, supercapacitors are admirable devices because of their efficiency, high energy and power density, quick charge - discharge rate and high stability and have become potential candidates in the area of energy storage devices [1-5]. However, most conventional supercapacitors are huge and weighty devices, restricting eventually their applications with regard to transportable electronic devices. In view of intense need for such transportable electronic devices like mobile phones and commercial electronics, it is essential to build up high-performance and authentic power sources that are small size, weightless, ease of handling, excellent reliability and safety. Inorganic materials are conducive for electrodes in supercapacitor and their physicochemical properties are closely associated to their morphology. The synthesis of inorganic materials based films with different morphologies and studies allow us to inspect their potentiality in different fields inclusive of supercapacitors [6-9] because of their porous structures and unique catalytic, optical, magnetic

and electrical properties [10-12]. It is in general the shape and size of materials matters in varying their optical, electrical and other properties. Thin film form of inorganic materials with a porous structure can offer a high surface area and are beneficial towards structural stability. These characteristics improve the electrochemical performance of films because they can facilitate sufficient access electrolyte ion into the active materials, shorten diffusion pathway and promote fast electron transfer [13-15]. In recent days, transition-metal phosphates, are eagerly studied as a novel electrode materials for next-generation supercapacitors, because of their strong three-dimensional $(P_2O_7)^{4-}$ matrix with more active sites for metal ions [16-18]. These materials have a high binding energy of oxygen renders excellent chemical durability and multidimensional path for ionic conduction [19]. The transition-metal phosphates doped with metal ions (such as Cu^{2+}, Zn^{2+}, Ni^{2+}, Mn^{4+}) have gained a great deal in recent years, which can favorably modify the properties of the materials by improving the overall electron density as well as electrical conductivity [20-22]. Vamsi Krishna *et al.* [23] synthesized nickel doped cobalt phosphate microarchitectures and explored electrochemical performance with results of high specific capacity of 108 mAh /g at 0.5 A /g. Na doped $Ni_2P_2O_7$-$Co_2P_2O_7$ with hierarchically porous bowknot-like structure has yielded a high specific capacity of 295.2 C /g at 2.0 A /g as explored by Wei et al. [24]. Priyadharshini et al. [25] prepared amorphous bimetallic $NiCoP_2O_7$/ g-C_3N_4 composite electrode and studied the supercapacitive properties, giving a specific capacitance of 342 F /g at a scan rate of 5 mV /s.

A facile approach to prepare ferrous nickel pyrophosphate ($Fe_2Ni_2P_2O_7$) thin film electrodes namely chemical bath deposition is adopted in the present work. The prepared $Fe_2Ni_2P_2O_7$ electrodes are investigated by the structural, optical, photoluminescence, Raman and electrochemical studies. The obtained results allow us to put forth the $Fe_2Ni_2P_2O_7$ electrodes as a promising material for energy storage devices.

2. Experimental section

2.1 Synthesis of ferrous nickel pyrophosphate thin films

Nickel chloride ($NiCl_2.6H_2O$), potassium dihydrogen orthophosphate (KH_2PO_4) and urea $CO(NH_2)_2$ are taken in 1:1:0.5 molar ratio in 70 ml deionized water kept in magnetic stirrer. They are mixed thoroughly at 1200 rpm at room temperature to achieve homogeneous solution formation. The pH of the solution is maintained as 9 and three separate baths are prepared with different ($FeCl_3$) concentrations viz., 1M, 2M and 3M.

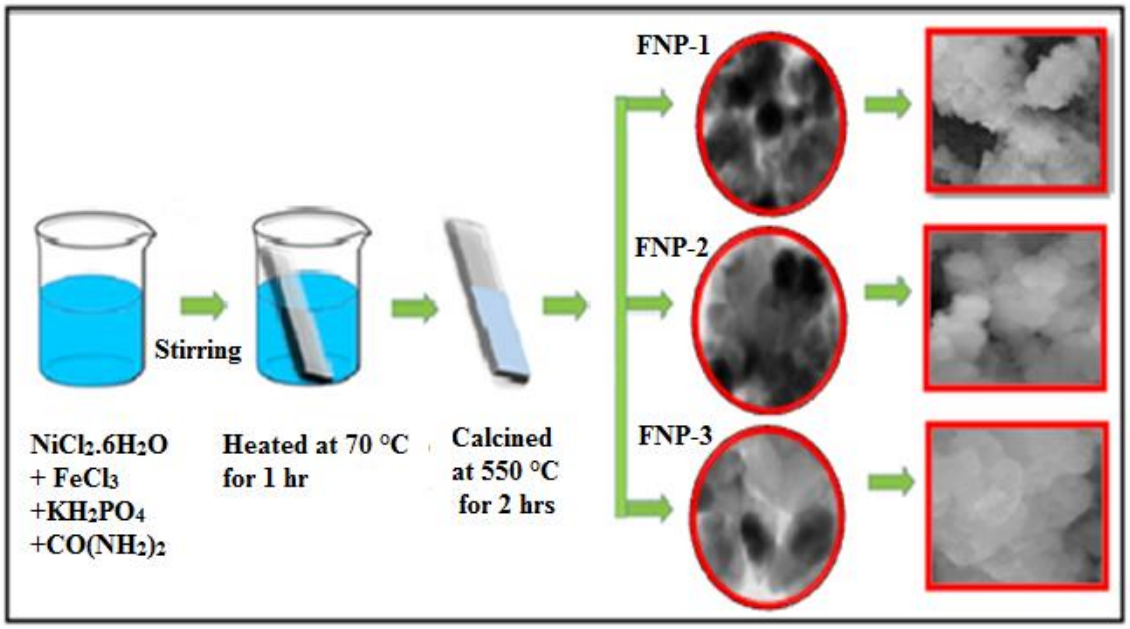

Figure 1. Schematic representation for synthesis of FNP thin films

The glass substrates are introduce into the baths at 70 °C and kept immersed for 1 hr. After the bath time, ferrous nickel pyrophosphate ($Fe_2Ni_2P_2O_7$) thin films labeled as FNP-1, FNP-2 and FNP-3 are found deposited uniformly on the glass substrates. Further, FNP thin films are rinsed with deionized water for 2 times so as to remove loosely binded material. Then the films are calcined at 550 °C for 2 hrs in a hot air oven and used for subsequent characterizations. Following is the reaction mechanism of Fe $_xNi_2P_2O_7$ (FNP) thin films (where x = 1M, 2M and 3M)

$$2[Ni(NH_3)_4]^{2+} + 2[Fe(NH_3)_6]^{2+} + 2H_2PO_4^- + nH_2O \rightarrow Fe_2Ni_2P_2O_7.nH_2O + 10NH_3 + H_2 \uparrow \quad (1)$$

2.2 Material Characterization

X-ray diffraction (XRD) of the prepared thin films are studied using Bruker D8 advance diffractometer with monochromatic Cu Kα radiation (λ=0.15425 nm). The scanning electron microscopy (SEM) images of prepared thin films are recorded by Hitachi S4800 and high resolution transmission electron microscopy (HR-TEM) of the best performed film is recorded by JEOL JEM-2100F. The surface areas of the prepared material are calculated by following Brunauer-Emmett-Teller (BET) analysis (Belsorp II mini). The chemical state and binding energy of prepared thin films are estimated by X-ray photoelectron spectroscopy (XPS) using ESCALAB 250 - Thermo Fisher Scientific. Optical properties of FNP thin films are studied by using UV-VIS Spectrophotometer (JASCO V-570). Photoluminescence is recorded at room temperature under the excitation wavelength of 280 nm using a fluorescence spectrometer (JASCO, FP-6500) equipped with a Xe lamp as the excitation light source. Raman spectroscopy is carried out by using a (InVia spectroscope – Renishaw) equipped with 514.5 nm light from Ar laser as the excitation source and obtained the structural changes of FNP films.

2.3 Electrochemical characterization

2.3.1 Fabrication of FNP working electrodes

The coated FNP thin film material are peeled off from the glass substrates and the working electrode comprises a mixture of the FNP as a active material (75 wt%), carbon black (20 wt%) and Polyvinylidene fluoride (5 wt%) are in N-Methyl-2-pyrrolidone solvent making a homogeneous slurry. The slurry is coated on a graphite foil current collector (2×2 cm^2) and dried at 80 °C for 10 h in a vacuum oven. The average mass loading of active material loaded ~2 mg on the graphite foil. The electrochemical properties of prepared FNP thin film electrodes are evaluated by cyclic voltammetry (CV), galvanostatic charge-discharge (GCD) and electrochemical impedance spectroscopy (EIS) is examined using BioLogic SP-300 modular electrochemical workstation at room temperature. The prepared FNP thin film as working electrode, a platinum wire as a counter electrode and Hg/HgO as a reference electrode are used as a typical three electrode system in 3M KOH as an electrolyte.

3. Results and discussion

3.1. Structural analysis

The X-ray diffraction pattern of FNP thin films are depicted in Figure 2. It is known from the XRD analysis that FNP thin films crystallized in monoclinic structure with space group $P2_{1/c}$ (14) which is indexed to JCPDS No: 83-0802. The Bragg reflections 2θ = 25.8°, 31.5°, 33.6°, 36.1°, 45.4°, 50.2° and 56.5° are attributed to (111), (013), (004), (211), (300), (115) and (313) planes respectively [26,27]. The preferential growth of the films is along the (111) direction and the preferred orientation factor f (111) of the (111) plane for the FNP films has been estimated by calculating the fraction of (111) plane intensity over the sum of intensities of all peaks within a measuring 2θ range from 20° to 80° (Table 1) [28]. All the diffraction peaks are sharp and no other impurity peaks are found in XRD pattern, which indicate that the films are highly crystalline in nature. The crystallographic parameters of FNP thin films are presented in the Table 1. The obtained crystallite size using Debye-Scherrer relation shows an increasing trend as 42.16 nm, 44.73 nm and 46.02 nm for FNP-1, FNP-2 and FNP-3, respectively. The increase in intensity of XRD peaks along with the increase in Fe concentration indicates the substitutional existence of Fe ions in the lattice with high crystallinity which would enhance electrochemical performance by virtue of its stable structure and maintaining the same during charge-discharge process [29].

Figure 3(a-f) depicts the SEM images of FNP thin films, which reveal the formation of microsphere like structure. It can be seen that microsphere in FNP-2, FNP-3 films are highly aggregated. The Fe concentration effect on the grain size and morphology is quite apparent in the SEM images showing growth and pattern change of aggregated microspheres. The grain size increases from a value of 40 nm to 50 nm in the range of Fe concentration (1M to 3M).

In view of the growth aspect in morphology as supported by HR-TEM images (Figure 4(a-d)). FNP-3 thin film stands first as the benefit of fast electron transport prevails and it would promote good charge storage. The HR-TEM images confirm the microsphere like morphology of the film with agglomeration [30, 31]. Figure. 4(c,d) depicts selected area electron diff raction (SAED) pattern displaying the diffraction fringes exhibits the high crystalline nature of the FNP-3 film. The d spacing value is 0.34 nm for (111) plane of the FNP-3 thin film belonging to monoclinic system respectively. The result of HR-TEM and XRD analysis compliment each other extracting the structural aspects of the thin films under study and highlight FNP-3 thin film.

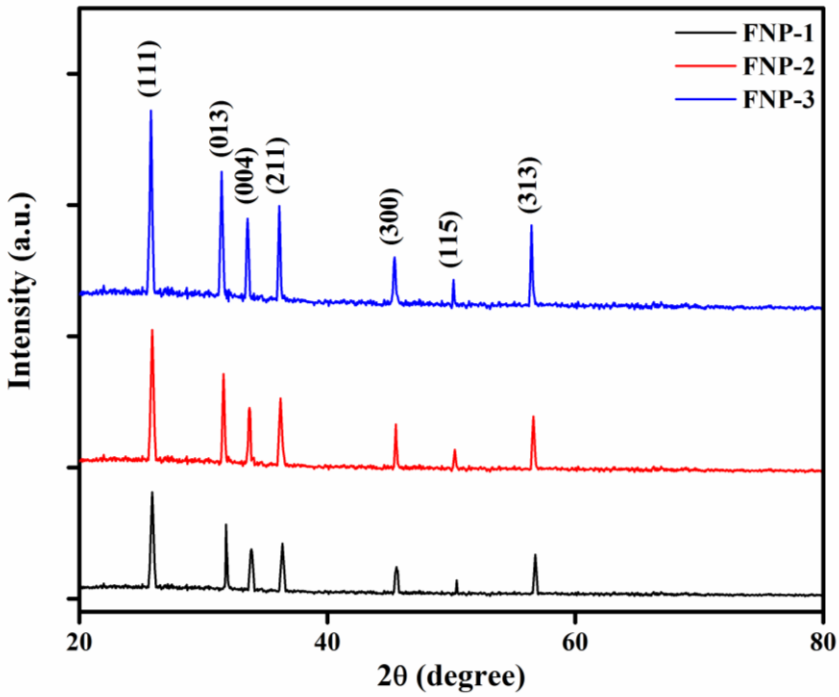

Figure 2. XRD pattern of FNP thin films

Table 1. The crystallographic parameters of FNP thin films

JCPDS No: 83-0802 (Monoclinic)	Unit cell parameters				Unit Cell volume (Å³)	Crystallite size (nm)	Orientation factor f (111) plane
	a (Å)	b (Å)	c (Å)	β (°)			
	5.99	4.73	10.37	90.89	294.27	-	
FNP-1film	6.01	4.73	10.27	90.20	294.37	42.16	0.3810
FNP-2 film	5.99	4.59	10.55	90.10	295.61	44.73	0.3859
FNP-3 film	5.93	4.81	10.39	91.46	296.31	46.02	0.3909

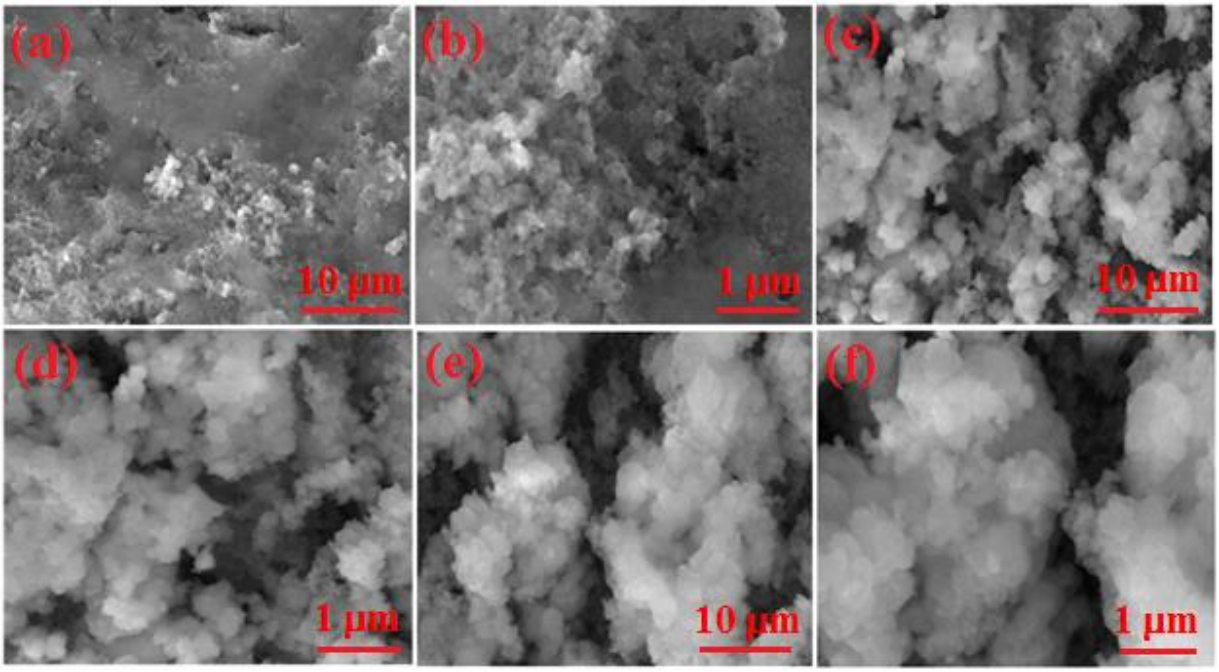

Figure 3. SEM images of (a, b) FNP-1, (c, d) FNP- 2 and (e, f) FNP-3 films at different magnification (X50000 and X100000)

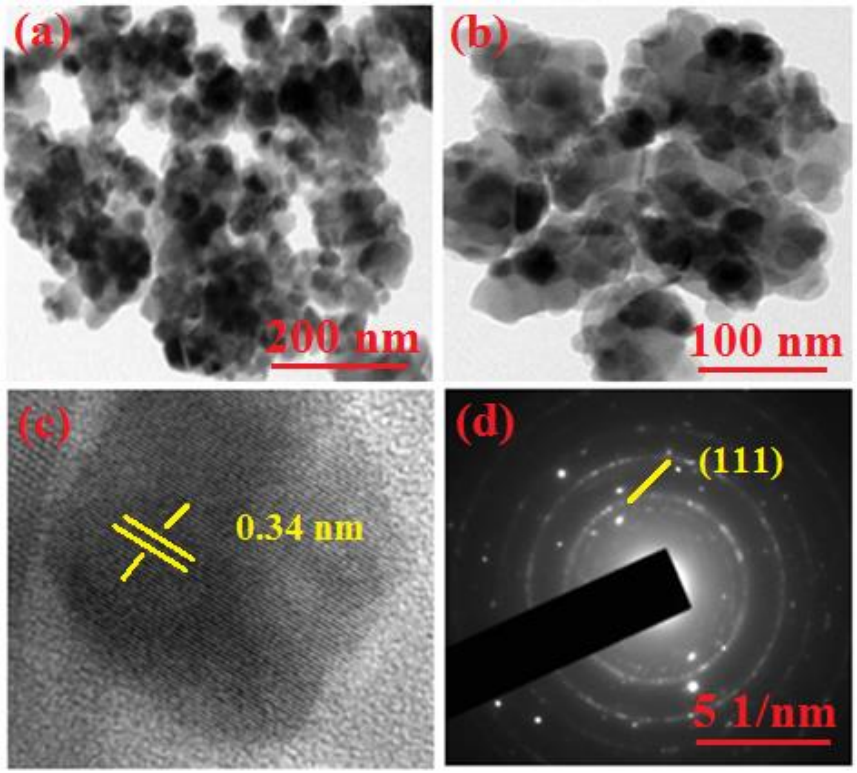

Figure 4. (a, b) HR-TEM images and (c, d) SAED pattern of FNP-3 thin film

Figure (5(a) and (b)) depicts the N_2 adsorption/desorption isotherms and the corresponding Barrett-Joyner-Halenda (BJH) pore size distribution curve of FNP thin films. The FNP-3 thin film shows improved N_2 adsorption than the FNP-1 and FNP-2 thin film. The BET surface area of FNP-1, FNP-2 and FNP-3 thin films are found to be 13.06 m^2/g, 19.4 m^2/g and 29.95 m^2/g, respectively (Figure 5(a)). Figure. 5(b) shows that the average pore diameters of FNP-1, FNP-2 and FNP-3 thin films are 3.93 nm, 4.65 nm and 6.05 nm respectively, which is attributed to the

microsphere like structure. The high surface area and high pore diameter of FNP-3 when compared with other film usually offers a more ion pathways for contact between the electrode and electrolyte interfaces and it is beneficial for high capacitive performance [16, 32].

Figure 6(a) shows the XPS survey spectra of FNP-3 thin film, which consist all elements such as Ni, Fe, P and O species. High resolution spectra of Ni 2p (Figure 6(b)) displays the two intense peaks at 857.5 eV and 875.3 eV binding energies are assigned to Ni $2p_{3/2}$ and Ni $2p_{1/2}$, respectively. In addition, the two satellite peaks at 862.9 eV and 881.6 eV can be attributed to oxidized Ni^{2+} species. XPS spectra of Fe 2p (Figure 6(c)) shows the binding energy located at 713.7 eV and 727.3 eV are assigned to the Fe $2p_{3/2}$ and Fe $2p_{1/2}$, respectively. Figure 6(d) shows XPS spectra of P 2p species, only one intense peak at 134.5 eV corresponds to P-O bonding. Moreover, the O 1s spectra shown in the Figure 6(e), the strong peak at 532.7 eV is associated with metal oxygen bonding in FNP-3 thin film. XPS results confirm the successful formation of FNP thin films, and support the XRD and FTIR analysis [29, 33, 34].

The optical absorbance spectra of FNP films obtained for the wavelength range 280-900 nm is shown in the Figure 7(a). The absorbance of FNP films sharply increases in UV region attaining maximum at 300 nm and gradually decreases in the stretch of longer wavelength in all the FNP films which differ with respect to Fe concentration. The transmittance spectra of FNP thin films are shown in Figure 7(b). It shows higher transparency of FNP-1 film in the near IR region with a transmittance of 78 % and the same decreases for other film in that region from 78 % - 45 % corresponding to the increase in Fe concentration from 1M to 3M as the density of atoms leads to optical scattering phenomenon in FNP thin films [35]. The gravimetric technique allows the determination of the thickness of FNP-1, FNP-2 and FNP-3 films and the values are 350 nm, 400 nm and 600 nm, respectively. The fall in transmittance is due to the increase in the thickness of films in which reflection of an incident light is caused by submicron particles [35, 36]. Figure 7(c) shows the plot of $(\alpha h\nu)^2$ versus $(h\nu)$ tauc plot for FNP thin films and the energy gap for these films are estimated by extrapolating the linear portion of the curve to energy axis. All the plots show straight line portions, which supports the interpretation of direct band gap for all the films. The band gap energy of FNP-1, FNP2 and FNP-3 are 3.80, 3.40 and 3.17 eV respectively and the band gap decrease with increase in Fe concentration in FNP films, and the Tauc plot analysis establishes the fact that the energy gap decreases with the Fe concentration as found in earlier works [37].

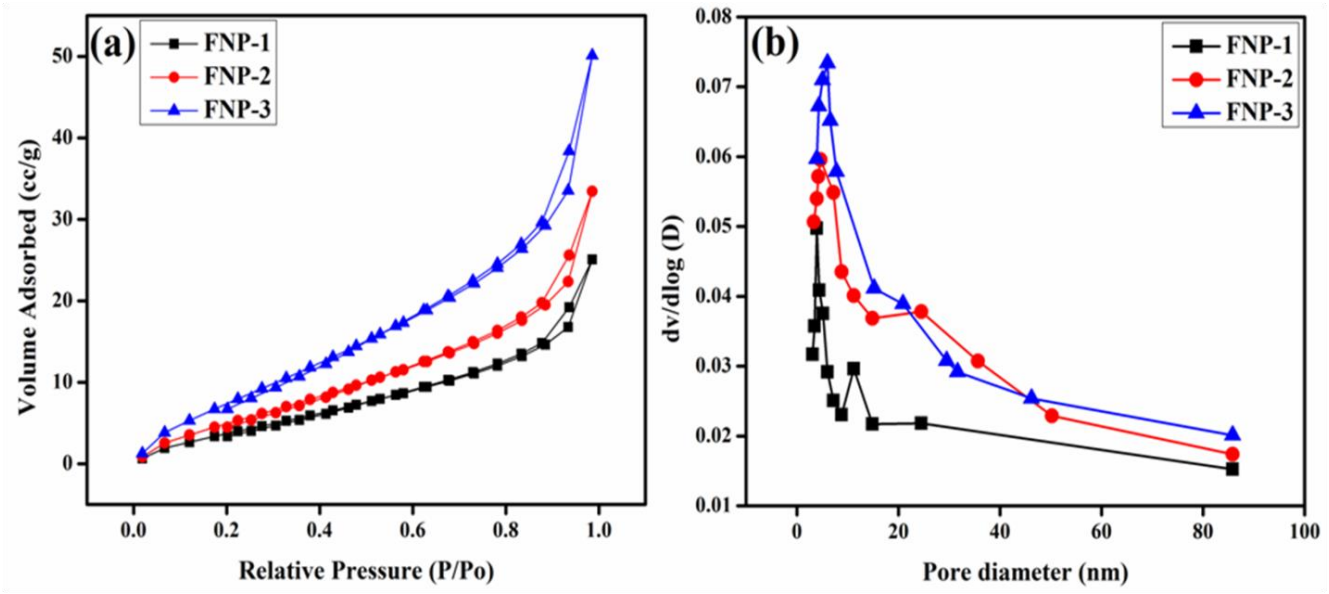

Figure 5 (a) N_2 adsorption – desorption isotherms (b) Pore size distribution curves of FNP thin films.

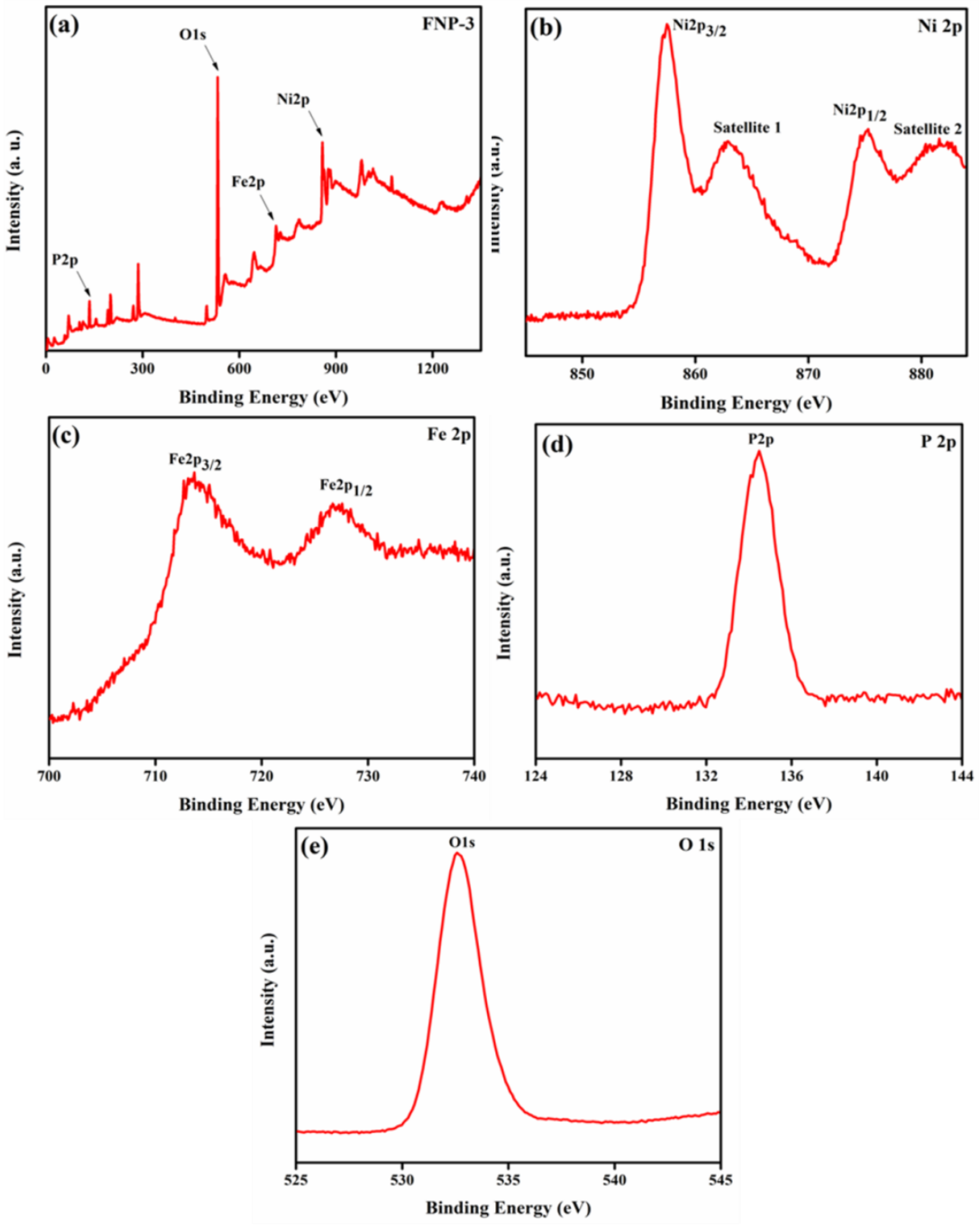

Figure 6 (a) XPS survey spectra (b) Ni 2p spectra (c) Fe 2p spectra (d) P 2p spectra and (e) O 1s spectra of FNP-3 thin film.

3.3. Photoluminescence studies

Figure 8 shows the PL emission spectra for FNP thin films excited at wavelength of 280 nm using source of Xenon lamp, in which three emission bands viz., ultraviolet, blue and green are produced. The UV emission peaks centered at 336, 346 and 362 nm are formed for the FNP films under study and the corresponding values of energy band gap (E_g) are 3.70, 3.59 and 3.40 eV. The less intense UV bands resulted in as the near band edge emission (NBE) due to the exciton recombination. The high intense blue emission peak located at 383 nm with E_g of 3.24 eV besides blue band emission of relatively short peaks at 410, 420 and 460 nm with corresponding E_g of 3.03, 2.96 and 2.70 eV are obtained. Higher the

intensity of PL band, greater is the content of surface oxygen, phosphate vacancies and other impurities. The both UV and blue bands are defects level emission caused by electron- hole recombination due to trap state or imperfection site [38]. Further the emission spectra record relatively less intense green emission at 491, 515 and 522 nm as a result of E_g as 2.53, 2.41 and 2.37 eV respectively. This green emission bands are due to the band to band transition involving Ni, Fe, P ions which confirms the metal, oxygen vacancies and other defects present on the surface of the FNP thin films [39].

3.3. Photoluminescence studies

Figure 8 shows the PL emission spectra for FNP thin films excited at wavelength of 280 nm using source of Xenon lamp, in which three emission bands viz., ultraviolet, blue and green are produced. The UV emission peaks centered at 336, 346 and 362 nm are formed for the FNP films under study and the corresponding values of energy band gap (E_g) are 3.70, 3.59 and 3.40 eV. The less intense UV bands resulted in as the near band edge emission (NBE) due to the exciton recombination. The high intense blue emission peak located at 383 nm with E_g of 3.24 eV besides blue band emission of relatively short peaks at 410, 420 and 460 nm with corresponding E_g of 3.03, 2.96 and 2.70 eV are obtained. Higher the intensity of PL band, greater is the content of surface oxygen, phosphate vacancies and other impurities. The both UV and blue bands are defects level emission caused by electron- hole recombination due to trap state or imperfection site [38]. Further the emission spectra record relatively less intense green emission at 491, 515 and 522 nm as a result of E_g as 2.53, 2.41 and 2.37 eV respectively. This green emission bands are due to the band to band transition involving Ni, Fe, P ions which confirms the metal, oxygen vacancies and other defects present on the surface of the FNP thin films [39].

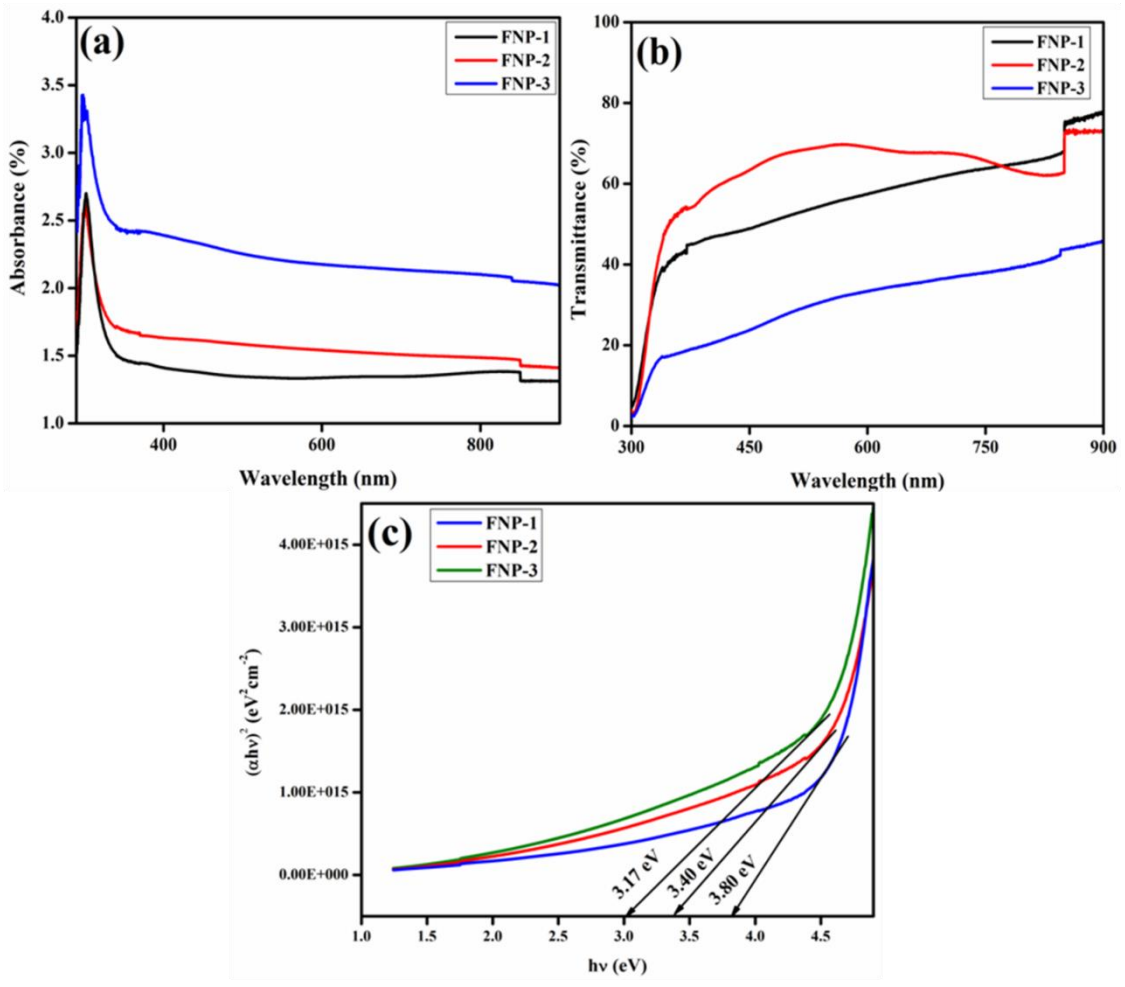

Figure 7 (a) Absorbance spectra (b) Transmittance spectra (c) Tauc plot of FNP thin films

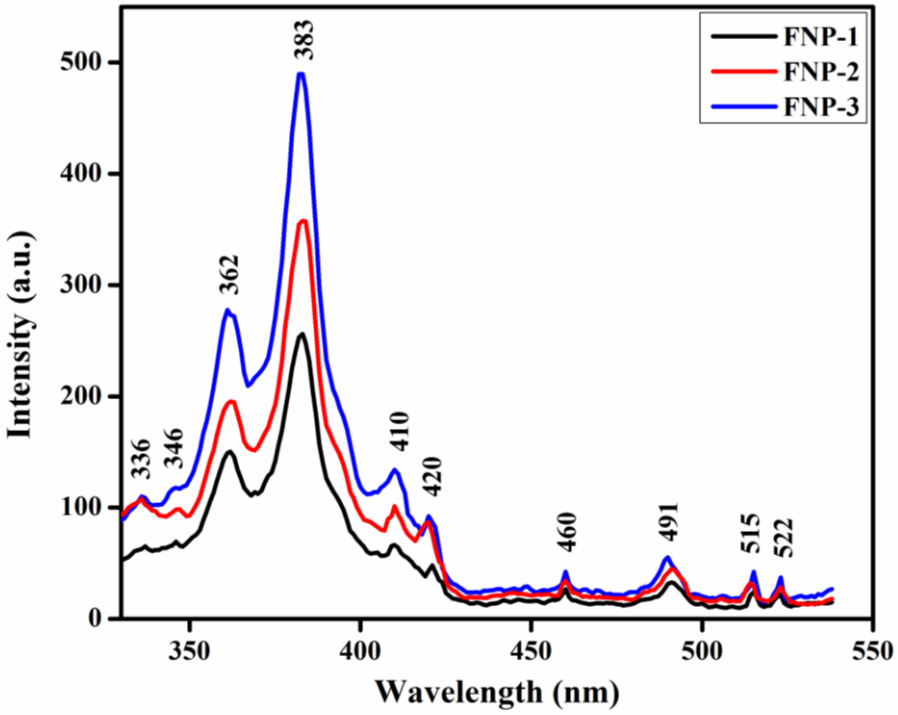

Figure 8 Photoluminescence spectra of FNP thin films

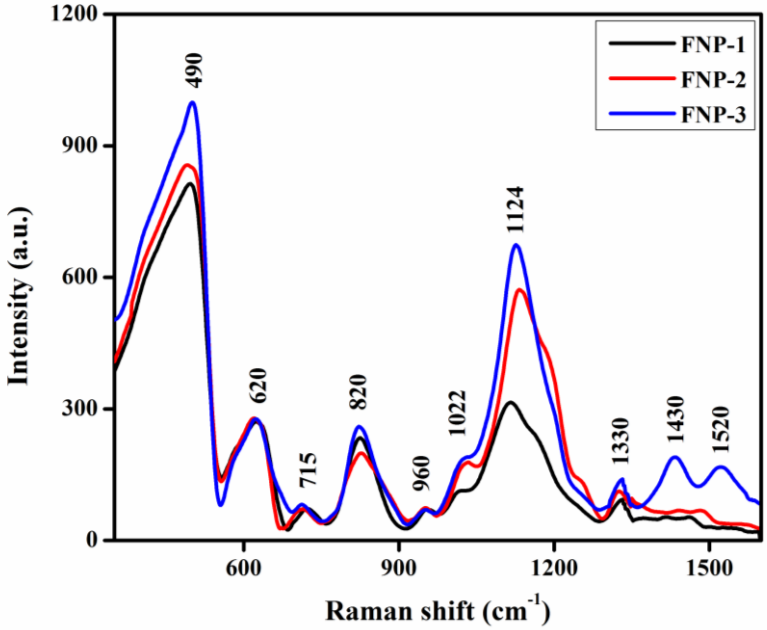

Figure 9 Raman spectra of FNP thin films

3.4. Raman analysis

Figure 9 shows the Raman vibrational spectra of FNP thin films in 350-1600 cm^{-1} region. Strong one phonon- magnon interaction (1P) peaks are observed as transverse optical mode (1TO) at ~ 490 cm^{-1} in all the spectral record and are assigned to the respective Ni-O symmetric modes with intense Raman activity. The Ni-O, Fe-O and P = O deformation takes place in the range between at 400 cm^{-1} and 1050 cm^{-1} and appear as (1TO, 1LO) and (2TO, TO+LO, 2LO) modes. The bending and torsional vibrations occur at 620 cm^{-1} and are assigned to the formation of mixed modes overlapping vibration involving iron- oxygen-polyhedral and $(P_2O_7)^{4-}$ groups [40, 41]. The weaker band located at

~715 cm^{-1} is due to the symmetric stretching vibration of P-O-P modes. The Raman bands at ~ 820, 960 and 1022 cm^{-1} are ascribed for symmetric stretching vibrations of Ni-O, Fe-O and P = 0 modes, respectively [44, 45]. The stronger two phonon (2P) peaks at ~1124 cm^{-1} are assigned to the respective O-P-O symmetric stretching modes with medium Raman activity and weaker 2P peaks are located at ~ 1330 cm^{-1} assigned to symmetric stretching mode Fe-O for FNP thin films. The two magnon (2M) peaks at ~ 1430 and 1520 cm^{-1} are assigned to the strong O-P-O symmetric stretching modes for FNP-3 thin film. The 2M modes appear in FNP-3 thin film because of high Fe concentration and strong O-P-O stretching modes are formed for FNP-3 films. The intensity of the Raman peaks increases upon increasing the molar concentration of Fe as clearly seen in the Raman spectra.

3.5. Electrochemical analysis

Figure 10(a-d) shows the CV curves of the FNP thin film electrodes at the different scan rates within the potential range of -0.4 to 0.2 V in 3M KOH as a electrolyte. The shapes of CV curves evince the pseudocapacitive behavior and all CV curves consist of redox peaks, which mainly results from the faradaic reaction of the Ni^{2+} to Ni^{3+} and Fe^{2+} to Fe^{3+} occurring at the surface of FNP electrode materials [44, 45]. The redox current increases when increasing the scan rate and also it is found that the redox peaks shift towards the right as well as the left of the potential window with a larger potential separation due to the resistance of electrode [45, 46]. The values of specific capacitance (C_s) of FNP electrodes are calculated from CV curve, using the following relations,

$$C_s = \frac{\int I\Delta V}{mv\Delta V} \quad (F/g) \qquad (1)$$

Where, C_s, $\int I\Delta V$, m, v and ΔV represent specific capacitance (F/g), integral area under the CV curve, active mass of the electrode (mg), scan rate (mV/s) and potential window (V), respectively. The calculated specific capacitance values are presented in Table 2. FNP-3 thin film shows the high specific capacitance value of 570 F/g at scan rate 10 mV/s, it is larger than that of FNP-1 and FNP-2. The result FNP-3 thin film electrode facilitates outstanding electrochemical performance.

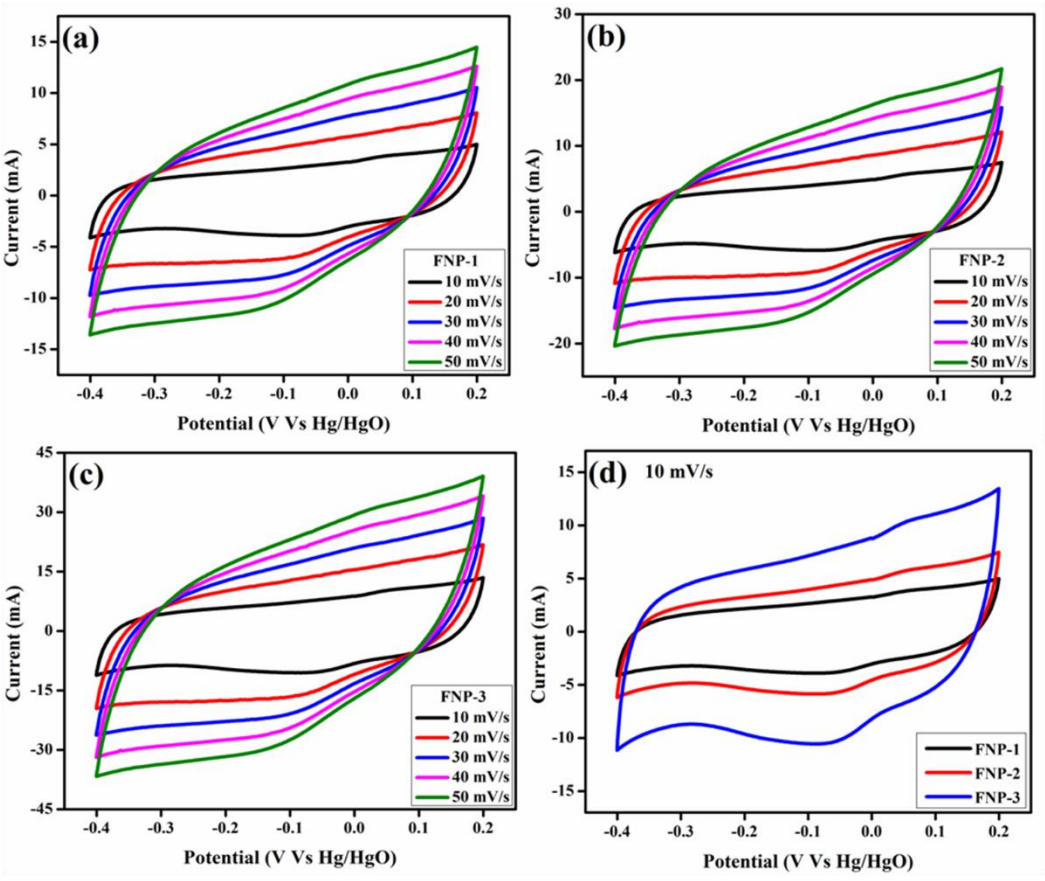

Figure 10 (a-d) CV curves of FNP thin films at different scan rates

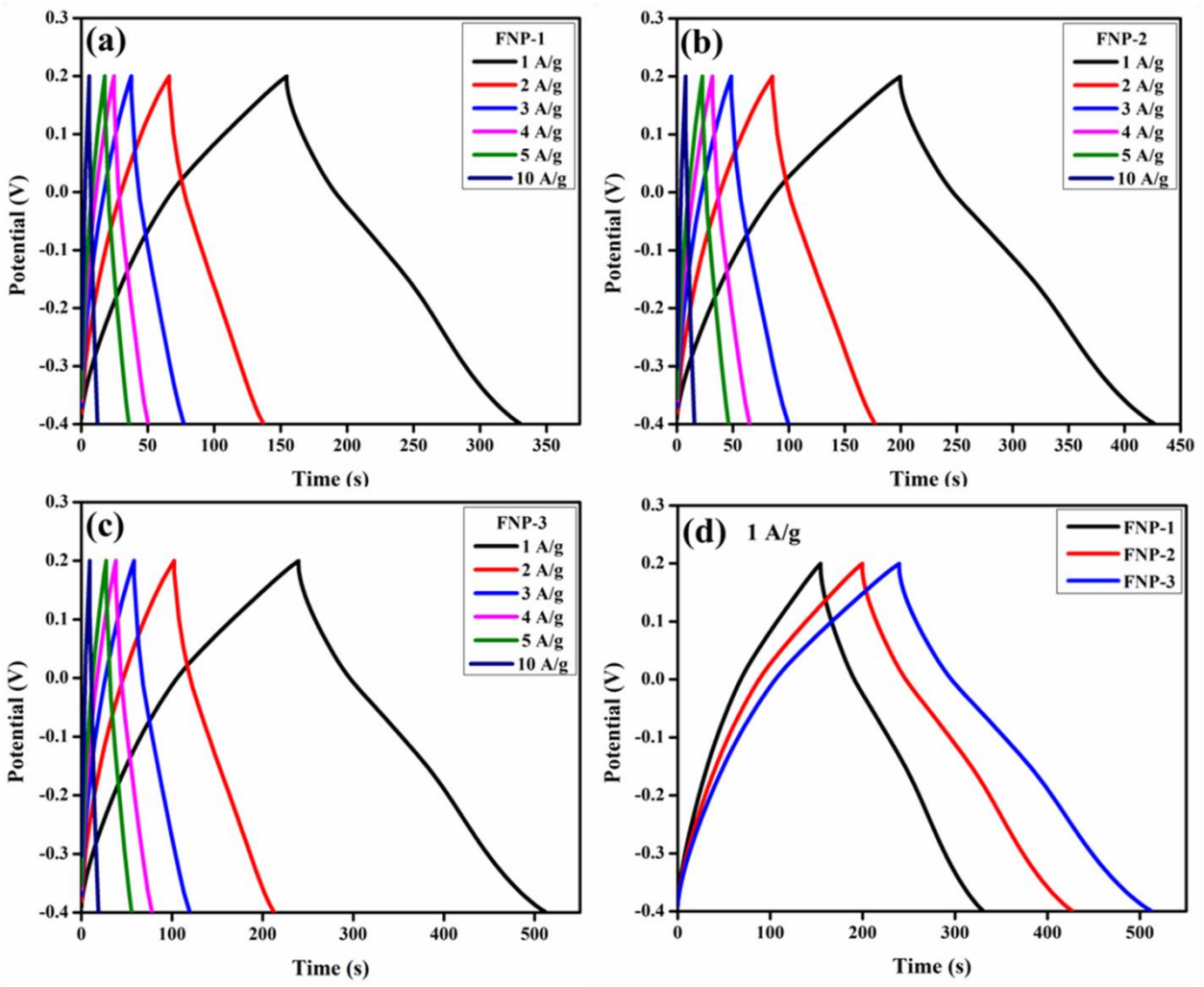

Figure 11 (a-d) GCD curves of FNP thin films at different current density

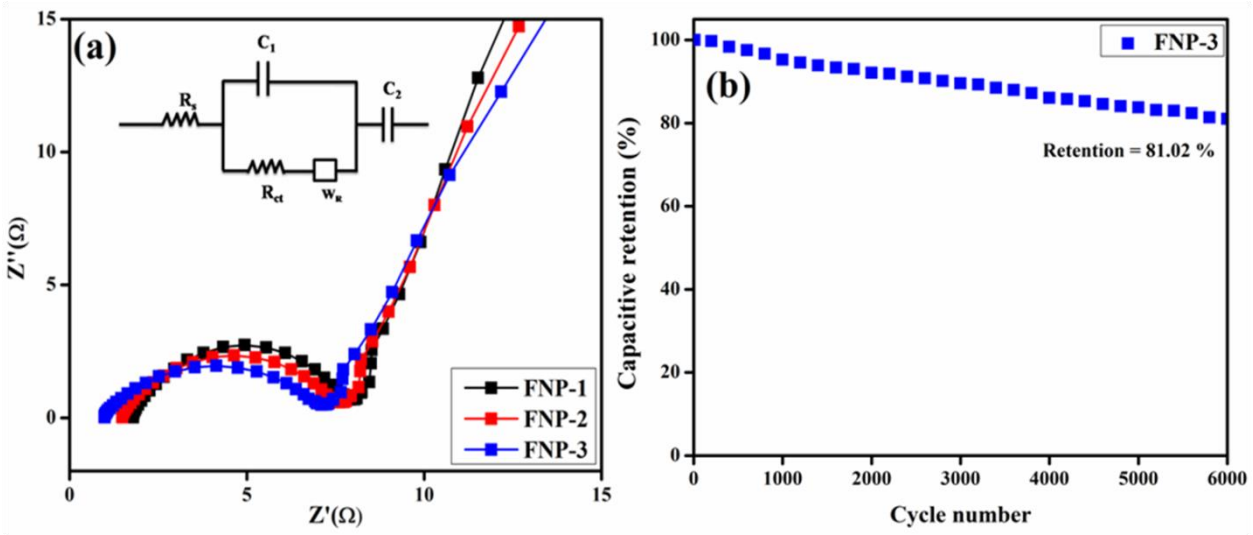

Figure 12 (a) Nyquist plot of FNP thin films (b) Capacitive retention of FNP-3 thin film.

Table 2. Specific capacitance of FNP thin film calculated from CV study

Thin film	Specific capacitance (F/g)				
	10 mV/s	**20 mV/s**	**30 mV/s**	**40 mV/s**	**50 mV/s**
FNP-1	387	301	228	172	141
FNP-2	487	393	283	213	181
FNP-3	570	475	414	322	247

Table 3. Specific capacitance of FNP thin film calculated from GCD study

Thin film	Specific capacitance (F/g)					
	1 A/g	**2 A/g**	**3 A/g**	**4 A/g**	**5 A/g**	**10 A/g**
FNP-1	323	264	205	143	119	21
FNP-2	387	307	269	177	146	49
FNP-3	441	370	340	260	239	92

Figure 11(a-d) depicts the measured charge-discharge curve of FNP electrodes at different current densities, all of which are non-linear in shape expressing the pseudocapacitive nature of the electrodes [24, 25, 47]. The GCD results are consistent with the CV tests. Based on the delivered charge-discharge time by the FNP electrodes, the specific capacitance values are calculated by the following equation [16]

$$C = \frac{I \times \Delta t}{m \times \Delta V} \quad (F/g) \qquad (2)$$

where, C represents the specific capacitance, I - the current (mA), Δt - the discharging time (s), ΔV - the operating potential (V) and m - the mass of the active material (mg). Notably that the discharge curves of FNP-3 exhibits prolonged discharge time than the FNP-1 and FNP-2 electrodes and corresponding changes in specific capacitance values of FNP electrodes are presented in Table 3. It is clearly visible that the specific capacitance values are enhanced by increasing the Fe concentration. The electrolytic ions have a plenty of time to diffuse into FNP electrodes, which leads to superior specific capacitance at lower current density.

To study the charge transfer kinetics and the resistance associated with the charge storage at the electrode/electrolyte interface, electrochemical impedance (EIS) spectroscopy is carried out in the frequency range of 100 mHz to 1 MHz and the Nyquist plot is shown in Figure 12(a). The Nyquist plot contains the solution resistance (R_s) which is associated with the resistance of electrolyte solution. The semicircle at the high frequency zone corresponds to the combination of charge-transfer resistance (R_{ct}) and capacitance (C) at the electrode/electrolyte interface. Further, linear line at low frequency zone is greater than 45° and towards to the imaginary axis is due to the diffusion of electrolyte ions on the electrode surface denoted as diffusion resistance (W) [42, 48]. Analyzing the Nyquist plot of FNP electrodes the charge-transfer resistance decreases in the order as FNP-1 > FNP-2 > FNP-3. The solution resistance (R_s) for FNP-1, FNP-2 and FNP-3 electrodes are found to be 1.79 Ω, 1.52 Ω and 1.02 Ω and charge transfer resistance (R_{ct}) are 6.27 Ω, 6.06 Ω and 5.90 Ω, respectively. The Nyquist plots reveal superior charge transfer kinetics of FNP-3, in the sense that FNP-1 and FNP-2 exhibit high access resistance and charge-transfer resistance compared to FNP-3. This put forth FNP-3 as ideal electrode that assist for enhanced electron transport during charge-discharge cycling. The long-term stability of the best performing FNP-3 electrode is tested for 6000 charge–discharge cycles and the cycle test recorded is shown in Figure 12(b). It exhibits excellent capacitance retention of 81.02 % even after 6000 cycles,

which ensure the outstanding electrochemical stability of the synthesized FNP-3 electrode. The observed superior specific capacitance, low impedance and outstanding electrochemical stability highlight FNP-3 as better electrode for supercapacitors.

4. Conclusion

In summary, $Fe_2Ni_2P_2O_7$ (FNP) thin film electrodes have been successfully developed by a facile chemical bath deposition method. All the FNP films have high crystalline nature with monoclinic structure. SEM, HR-TEM and BET results show that the films are composed of well defined microspheres with agglomeration with high surface area and grain size increases from 40 nm to 50 nm with increase in Fe concentration from 1M to 3M. The XPS results confirms formation $Fe_2Ni_2P_2O_7$ material by observing metal phosphate content and their corresponding bonds in the prepared films. Optical analysis reveals decreasing trend in direct optical band gap of FNP films as to be from 3.80 eV to 3.17 eV with increasing Fe concentration from 1M to 3M and obviously the band gap decreases with level of Fe concentation. The PL spectra confirm that all the films have high intense blue emission at 383 nm with band gap of 3.24 eV, which is supported by optical studies. Raman analysis reveals the phase purity of FNP thin films. The as-prepared FNP-3 thin film electrode shows an improved specific capacitance of 441 F/g at current density 1 A/g, when compared to the other two electrodes namely FNP-1 and FNP-2. It also exhibits a longer lifetime, capacitance retention of 81.02 % even after 6000 cycles and remarkable electrochemical properties. The characterization studies of FNP films put forward the FNP-3 as a promising candidate for energy storage devices and relevant applications.

References

[1] Y. Xiao, A. Zhang, S. Liu, J. Zhao, S. Fang, D. Jia, F. Li, Free-standing and porous hierarchical nanoarchitectures constructed with cobalt cobaltite nanowalls for supercapacitors with high specific capacitances. J*ournal of Power Sources*, *219*, (2012) 140-146. https://doi.org/10.1016/j.jpowsour.2012.07.030

[2] H. Wang, Q. Hao, X. Yang, L. Lu, X. Wang, Graphene oxide doped polyaniline for supercapacitors. Electrochemistry Communications, 11(6), (2009) 1158-1161. https://doi.org/10.1016/j.elecom.2009.03.036

[3] G. Zhu, C. Xi, Y. Liu, J. Zhu, X. Shen, (2015). CN foam loaded with few-layer graphene nanosheets for high-performance supercapacitor electrodes. Journal of Materials Chemistry A, 3(14), 7591-7599. https://doi.org/10.1039/C5TA00837A

[4] Y. Fu, J. Song, Y. Zhu, C. Cao, High-performance supercapacitor electrode based on amorphous mesoporous Ni (OH) 2 nanoboxes. Journal of Power Sources, 262, (2014) 344-348. https://doi.org/10.1016/j.jpowsour.2014.04.002

[5] T. Brousse, D. Bélanger, J.W. Long, To be or not to be pseudocapacitive?. Journal of The Electrochemical Society, 162(5), (2015) A5185. https://doi.org/10.1149/2.0201505jes

[6] C. Wei, Q. Lu, J. Sun, F. Gao, Evolution of nickel sulfide hollow spheres through topotactic transformation. Nanoscale, 5(24), (2013) 12224-12230. https://doi.org/10.1039/C3NR03371F

[7] M. Cao, T. Liu, S. Gao, G. Sun, X. Wu, C. Hu, Z.L. Wang, Single-crystal dendritic micro-pines of magnetic α-Fe2O3: large-scale synthesis, formation mechanism, and properties. Angewandte Chemie Angewandte Chemie, 44(27), (2005) 4197-4201. https://doi.org/10.1002/ange.200500448

[8] C. Wei, H. Pang, B. Zhang, Q. Lu, S. Liang, F. Gao, Two-dimensional β-MnO2 nanowire network with enhanced electrochemical capacitance. Scientific reports, 3(1), (2013) 2193. https://doi.org/10.1038/srep02193

[9] B. Geng, B. Tao, X. Li, W. Wei, Ni^{2+}/surfactant-assisted route to porous α-Fe_2O_3 nanoarchitectures. Nanoscale, 4(5), (2012) 1671-1676. https://doi.org/10.1039/c2nr12102f

[10] Y. Ni, K. Liao, J. Hong, X. Wei, (2009). Ni^{2+} ions assisted hydrothermal synthesis of flowerlike Co^{11} $(HPO_3)_8(OH)_6$ superstructures and shape control. *CrystEngComm*, *11*(4), 570-575. https://doi.org/10.1039/b819286c

[11] L. Liao, Q. Cao, H. Liao, Investigation of a hyperbranched polyurethane as a solid-state phase change material. Journal of materials

science, 45, (2010) 2436-2441. https://doi.org/10.1007/s10853-010-4211-3

[12] H. Pang, Y. Liu, J. Li, Y. Ma, G. Li, Y. Ai, J. Chen, J. Zhang, H. Zheng, Cobalt phosphite microarchitectures assembled by ultralong nanoribbons and their application as effective electrochemical capacitor electrode materials. Nanoscale, 5(2), (2013) 503-507. https://doi.org/10.1039/C2NR32597G

[13] X. Li, S. Xiong, J. Li, J. Bai, Y. Qian, Mesoporous NiO ultrathin nanowire networks topotactically transformed from α-Ni (OH) 2 hierarchical microspheres and their superior electrochemical capacitance properties and excellent capability for water treatment. Journal of Materials Chemistry, 22(28), (2012) 14276-14283. https://doi.org/10.1039/c2jm32559d

[14] J. Zhu, Z. Yin, D. Yang, T. Sun, H. Yu, H.E. Hoster, H.H. Hng, H. Zhang, Q. Yan, Hierarchical hollow spheres composed of ultrathin Fe_2O_3 nanosheets for lithium storage and photocatalytic water oxidation. Energy & Environmental Science, 6(3), (2013) 987-993. https://doi.org/10.1039/c2ee24148j

[15] A. Pan, T. Zhu, H.B. Wu, X.W. Lou, Template-Free Synthesis of Hierarchical Vanadium-Glycolate Hollow Microspheres and Their Conversion to V_2O_5 with Improved Lithium Storage Capability. Chemistry–A European Journal, 19(2), (2013) 494-500. https://doi.org/10.1002/chem.201203596

[16] S.J. Marje, P.K. Katkar, S.S. Pujari, S.A. Khalate, P.R. Deshmukh, U.M. Patil, (2020). Effect of phosphate (anion) precursor on structural and morphology behavior of nickel phosphate thin films and its supercapacitive performance. *Materials Science and Engineering: B*, *261*, 114641. https://doi.org/10.1016/j.mseb.2020.114641

[17] M. Liu, J. Li, W. Han, L. Kang, Simple synthesis of novel phosphate electrode materials with unique microstructure and enhanced supercapacitive properties. *Journal of energy chemistry*, *25*(4), (2016) 601-608. https://doi.org/10.1016/j.jechem.2016.03.002

[18] J. Theerthagiri, K. Thiagarajan, B. Senthilkumar, Z. Khan, R.A. Senthil, P. Arunachalam, J. Madhavan, M. Ashokkumar, Synthesis of hierarchical cobalt phosphate nanoflakes and their enhanced electrochemical performances for supercapacitor applications. ChemistrySelect, 2(1), (2017) 201-210. https://doi.org/10.1002/slct.201601628

[19] B. Senthilkumar, Z. Khan, S. Park, K. Kim, H. Ko, Y. Kim, Highly porous graphitic carbon and $Ni_2P_2O_7$ for a high performance aqueous hybrid supercapacitor. Journal of Materials Chemistry A, 3(43), (2015) 21553-21561. https://doi.org/10.1039/C5TA04737D

[20] T.N. Lambert, D.J. Davis, W. Lu, S.J. Limmer, P.G. Kotula, A. Thuli, M. Hungate, G. Ruan, Z. Jin, J.M. Tour, Graphene–Ni–α-MnO_2 and –Cu–α-MnO_2nanowire blends as highly active non-precious metal catalysts for the oxygen reduction reaction. *Chemical Communications*, *48*(64), (2012) 7931-7933. https://doi.org/10.1039/c2cc32971a

[21] A. Anis Fathima, S. Nivetha, S. Prabahar, S. Srikanth, R.T. Karunakaran, U. Karunanithi, M. Narendhera Ganth, Optical Study of Copper Zinc Tin Sulfide Thin Films by Chemical Bath Deposition Technique. International Journal for Research in Applied Science & Engineering, 9(3), (2021) 242-245.

[22] J. Yang, C. Zheng, P. Xiong, Y. Li, M. Wei, (2014). Zn-doped Ni-MOF material with a high supercapacitive performance. Journal of Materials Chemistry A, 2(44), 19005-19010. https://doi.org/10.1039/C4TA04346D

[23] B.V. Krishna, S.K. Hussain, J.S. Yu, (2021). Three-dimensional flower-like nickel doped cobalt phosphate hydrate microarchitectures for asymmetric supercapacitors. Journal of Colloid and Interface Science, 592, 145-155. https://doi.org/10.1016/j.jcis.2021.02.040

[24] C. Wei, S. Yang, W. Liu, X. Hou, Y. Sun, J. Zhao, W. Xiong, C. Cheng, D. Zhang, 2019. Hierarchically porous bowknot-like sodium doped $Ni_2P_2O_7$-$Co_2P_2O_7$ with improved supercapacitor performances. Applied Surface Science, 465, 763-771. https://doi.org/10.1016/j.apsusc.2018.09.223

[25] P. Matheswaran, P. Karuppiah, S.M. Chen, P. Thangavelu, B. Ganapathi, Fabrication of g-C3N4 nanomesh-anchored amorphous NiCoP2O7: tuned cycling life and the dynamic behavior of a hybrid capacitor. ACS omega, 3(12), (2018)

18694-18704. https://doi.org/10.1021/acsomega.8b02635

[26] J.K. Warner, A.K. Cheetham, D.E. Cox, Determination of the cation distribution in $NiFe_2(PO_4)_2$ using resonant X-ray and neutron powder diffraction. Journal of applied crystallography, 28(5), (1995) 494-502.

[27] S. Nivetha, S. Prabahar, R.T. Karunakaran, M.N. Ganth, S. Dhinesh, Synthesis and characterization of $Ni_2P_2O_7$ thin film as a superior electrode material for high performance supercapacitors. *Ionics*, *29*(3), (2023) 1209-1219. https://doi.org/10.1007/s11581-023-04885-4

[28] S. Prabahar, M. Dhanam, CdS thin films from two different chemical baths-structural and optical analysis. *Journal of Crystal growth*, *285*(1-2), (2005) 41-48. https://doi.org/10.1016/j.jcrysgro.2005.08.008

[29] Y. Liu, Y.X. Yu, W.D. Zhang, (2012). Photoelectrochemical properties of Ni-doped Fe2O3 thin films prepared by electrodeposition. *Electrochimica acta*, *59*, 121-127. https://doi.org/10.1016/j.electacta.2011.10.051

[30] F.S. Omar, A. Numan, S. Bashir, N. Duraisamy, R. Vikneswaran, Y.L. Loo, K. Ramesh, S. Ramesh, Enhancing rate capability of amorphous nickel phosphate supercapattery electrode via composition with crystalline silver phosphate. *Electrochimica Acta*, *273*, (2018) 216-228. https://doi.org/10.1016/j.electacta.2018.03.136

[31] M. Priyadharshini, T. Pazhanivel, G. Bharathi, Carbon quantum dot incorporated nickel pyrophosphate as alternate cathode for supercapacitors. *ChemistrySelect*, *5*(8), (2020) 2643-2652. https://doi.org/10.1002/slct.201904334

[32] S. Dhinesh, M. Priyadharshini, T. Pazhanivel, R. Gobi, Biomass-derived N, S self-doped activated carbon embedded MnO_2 as cathode for supercapacitor.*Materials Technology*, *37*(11), (2022) 1837-1845. https://doi.org/10.1080/10667857.2021.1990458

[33] S. Nivetha, S. Prabahar, R.T. Karunakaran, M.N. Ganth, T. Boobalan, S. Dhinesh, Improved Electrochemical Performance of $Ni_2P_2O_7$ and Mn-doped $Ni_2P_2O_7$ Electrode Materials for Supercapacitor Applications. ChemistrySelect, 8(20), (2023), e202300535. https://doi.org/10.1002/slct.202300535

[34] S. Dhinesh, M. Priyadharshini, T. Pazhanivel, R. Gobi, Biomass-derived N, S self-doped activated carbon embedded MnO_2 as cathode for supercapacitor. *Materials Technology*, *37*(11), (2022) 1837-1845. https://doi.org/10.1021/acs.chemmater.6b01522

[35] C.R. Dhas, R. Venkatesh, R. Sivakumar, A.M.E. Raj, C.J.O.M. Sanjeeviraja, Effect of solution molarity on optical dispersion energy parameters and electrochromic performance of Co_3O_4 films.*Optical Materials*, *72*, (2017) 717-729. https://doi.org/10.1016/j.optmat.2017.07.026

[36] S. Nivetha, S. Prabahar, R.T. Karunakaran, M. Narendhera Ganth, S. Dhinesh, $Ni_2P_2O_7$ Thin Film Electrode for High Performance Supercapacitor Applications. *International Journal for Research in Applied Science & Engineering Technology*, 11(7), (2023), 979-982. https://doi.org/10.22214/ijraset.2023.54766

[37] Y. Zhao, H. Wang, C. Wu, Z.F. Shi, F.B. Gao, W.C. Li, G.G. Wu, B.L. Zhang, G.T. Du, Structures, electrical and optical properties of nickel oxide films by radio frequency magnetron sputtering. *Vacuum*, *103*, (2014) 14-16. https://doi.org/10.1016/j.vacuum.2013.11.009

[38] R. Murugesan, S. Sivakumar, K. Karthik, P. Anandan, M. Haris, Structural, optical and magnetic behaviors of Fe/Mn-doped and co-doped CdS thin films prepared by spray pyrolysis method. *Applied Physics A*, *125*, (2019) 1-13. https://doi.org/10.1007/s00339-019-2577-x

[39] S. Narayanan, J.J. Vijaya, T. Adinaveen, M. Bououdina, L.J. Kennedy, Synthesis of α-Fe_2O_3 sphere/rod-like nanostructure via simple surfactant-free precipitation route: optical properties and formation mechanism. *Journal of Nanoscience and Nanotechnology*, *15*(6), (2015) 4558-4566. https://doi.org/10.1166/jnn.2015.9614

[40] M.N. Ganth, S. Prabahar, R.T. Karunakaran, S. Nivetha, S. Dhinesh, Facile synthesis of cobalt phosphate electrode material for enhanced electrochemical supercapacitor applications. *Ionics*, *29*(8), (2023) 3261-3271. https://doi.org/10.1007/s11581-023-05065-0

[41] Y.M. Lai, X.F. Liang, S.Y. Yang, J.X. Wang, B.T. Zhang, Raman spectra study of iron phosphate

glasses with sodium sulfate. *Journal of Molecular Structure*, *1013*, (2012) 134-137. https://doi.org/10.1016/j.molstruc.2012.01.025

[42] Y.M. Lai, X.F. Liang, S.Y. Yang, J.X. Wang, L.H. Cao, B. Dai, Raman and FTIR spectra of iron phosphate glasses containing cerium. *Journal of Molecular Structure*, *992*(1-3), (2011) 84-88. https://doi.org/10.1016/j.molstruc.2011.02.049

[43] P. Stoch, W. Szczerba, W. Bodnar, M. Ciecinska, A. Stoch, E. Burkel, Structural properties of iron-phosphate glasses: spectroscopic studies and ab initio simulations. *Physical Chemistry Chemical Physics*, *16*(37), (2014) 19917-19927. https://doi.org/10.1039/C4CP03113J

[44] S. Nivetha, S. Prabahar, R.T. Karunakaran, M.N. Ganth, S. Dhinesh, Effect of Fe dopant concentration on electrochemical properties of $Ni_2P_2O_7$ thin films. Inorganic Chemistry Communications, 146, (2022) 110193. https://doi.org/10.1016/j.inoche.2022.110193

[45] C. Wei, C. Cheng, S. Wang, Y. Xu, J. Wang, H. Pang, Sodium-doped mesoporous $Ni_2P_2O_7$ hexagonal tablets for high-performance flexible all-solid-state hybrid supercapacitors. *Chemistry–An Asian Journal*, *10*(8), (2015) 1731-1737. https://doi.org/10.1002/asia.201500335

[46] J. Yan, W. Sun, T. Wei, Q. Zhang, Z. Fan, F. Wei, Fabrication and electrochemical performances of hierarchical porous $Ni(OH)_2$ nanoflakes anchored on graphene sheets. *Journal of Materials Chemistry*, *22*(23), (2012) 11494-11502. https://doi.org/10.1039/c2jm30221g

[47] S. Nivetha, S. Prabahar, R.T. Karunakaran, M.N. Ganth, S. Dhinesh, Synthesis and characterization of $Ni_2P_2O_7$ thin film as a superior electrode material for high performance supercapacitors. *Ionics*, *29*(3), (2023) 1209-1219. https://doi.org/10.1007/s11581-023-04885-4

[48] S. Kaipannan, S. Marappan, Fabrication of 9.6 V High-performance Asymmetric Supercapacitors Stack Based on Nickel Hexacyanoferrate-derived $Ni(OH)_2$ Nanosheets and Bio-derived Activated Carbon. *Scientific Reports,* 9(2019), 1104. https://doi.org/10.1038/s41598-018-37566-8

Does this article screened for similarity?
Yes

Author Contribution Statement
S. Nivetha - Methodology, Investigation, Writing- Original draft preparation. **S. Prabahar**- Conceptualization, Supervision, Writing- Reviewing and Editing. **R. T. Karunakaran** -Writing- Reviewing and Editing. **M. Nardheraganth**- Formal Analysis Data Curation. **S. Dhinesh**- Formal Analysis, Writing- Original draft preparation. **T. Boopalan**- Software, Investigation, Writing- Original draft preparation. All the authors read and approved the final version of the manuscript.

Conflict of interest
The Authors declares that there is no conflict of interest anywhere.

More Information
This article was part of the Second National Conference on Emerging Materials for a Sustainable Future (https://www.psgtech.edu/educms/sorces/CLG/anns/Brochure%20NCEMSF%202024.pdf), held on July 25–26, 2024, and organized by the Department of Physics, PSG College of Technology, Coimbatore, India.
Title: Proceedings of the Asian Research Association
Journal Abbreviation: Proc. Asian Res. Assoc.
Publication language: English
Publishing Frequency: Continuously updated
Month of Publication: July, 2024
Subject: Physical Sciences, Chemical Sciences, Engineering, Environmental Science.

How to cite this article
Nivetha, S., Prabahar, S., Karunakaran, R. T., Boobalan, T., & Dhinesh, T. (2024). Electrochemical Properties of Ferrous Nickel Pyrophosphate Thin Film Electrodes for Energy Storage Applications. Proceedings of the Asian Research Association, 1(1), 71-86. doi: 10.54392/ara2417.

About the License